Absorbing boundary conditions for the time-dependent Schrödinger-type equations in $\mathbb{R}^3$

Xiaojie Wu*
Department of Mathematics, University of California, Berkeley, California 94720, USA

Xiantao Li†
Department of Mathematics, The Pennsylvania State University, University Park, Pennsylvania 16802, USA

(Received 9 August 2019; published 8 January 2020)

Absorbing boundary conditions are presented for three-dimensional time-dependent Schrödinger-type of equations as a means to reduce the cost of the quantum-mechanical calculations. The boundary condition is first derived from a semidiscrete approximation of the Schrödinger equation with the advantage that the resulting formulas are automatically compatible with the finite-difference scheme and no further discretization is needed in space. The absorbing boundary condition is expressed as a discrete Dirichlet-to-Neumann map, which can be further approximated in time by using rational approximations of the Laplace transform to enable a more efficient implementation. This approach can be applied to domains with arbitrary geometry. The stability of the zeroth-order and first-order absorbing boundary conditions is proved. We tested the boundary conditions on benchmark problems. The effectiveness is further verified by a time-dependent Hartree-Fock model with Skyrme interactions. The accuracy in terms of energy and nucleon density is examined as well.

DOI: 10.1103/PhysRevE.101.013304

I. INTRODUCTION

Quantum-mechanical simulations, expressed in terms of the Schrödinger equation, provide a fundamental description of physical properties in chemistry and condensed-matter physics [1,2]. On the other hand, due to the small length scale, an outstanding challenge is the size of the system that one can simulate, even with the rapid growth of computing power. Computer simulations often face the scenarios where the electrons are being emitted out of the computational domain, e.g., the photoionization process. Recently there has been a great deal of renewed interest in such issues in the quantum transport problem [3], optical response of molecules [4], open quantum systems [5], etc.

One approach to address the aforementioned issue is by absorbing boundary conditions (ABCs) which reduce the problem to a much smaller computational domain and yield results as if the simulation is being performed in a much larger (or unbounded) domain. Rather than simply removing the exterior region, the ABCs provide an efficient approach to mimic the influence from the surrounding environment. There are several different approaches to construct and implement ABCs, most of which involve the derivation and approximation of the Dirichlet-to-Neumann (DtN) map. They are also commonly referred to as nonreflecting, transparent, or radiating boundary conditions. By replacing the surrounding region with the ABCs, the computational effort can be focused on simulating the region of interest.

There seemed to be separate development of ABCs for quantum-mechanical simulations. For example, there is a great deal of progress in developing ABCs in physics and chemistry. These ABCs can be roughly classified into four approaches: (1) the exterior complex scaling (ECS) [6–9], where the coordinate outside a fixed radius is scaled into the complex plane; (2) the mask function method [10–12], where the wave functions are gradually scaled to zero; (3) complex absorbing potentials (CAP) [13–15], which is introduced outside the boundary by adding a complex potential to the Hamiltonian; and (4) coordinate scaling, which scales the spatial coordinate by a time-dependent factor [16,17] to make wave functions compatible with the physical boundary conditions. These methods are not constructed to directly approximate the exact boundary condition. Rather, they are very much goal oriented. Their direct aim is to absorb the electrons that move outside the computational domain. These methods in general are easy to implement and are quite robust in practice. Meanwhile, the effectiveness depends heavily on the choice of the parameters, e.g., in the CAP methods, the size of the boundary region and the magnitude of the potential. In some cases, the efficiency and accuracy (reflections) are even debatable for decades [18–22]. The ABCs can also be introduced for the density-matrix in the Liouville von-Neumann equation [23].

In the applied math community, much effort has been focused on one-dimensional (1D) problems, with a few works for multidimensional problems with flat boundary, for a comprehensive review, see Refs. [24,25]. There a different path is followed: The *exact* ABCs are first derived by solving an exterior problem, many of which are written as a DtN or Neumann-to-Dirichlet (NtD) map for the continuous time-dependent Schrödinger equation (TDSE) [26] (or temporally

*xiaojiewu@berkeley.edu
†xxl12@psu.edu

discrete model [27], spatially discrete model [28,29], and fully discrete model [30]). The same technique has been used by Ermolaev *et al.* [31,32] to treat electron dynamics under a laser field, where the exact boundary condition, referred to as an integral boundary condition, is derived with the help of the Green's function for a free electron. Then, the exact ABCs, which involve a time convolution, are approximated to avoid the repeated calculations of the integrals. The most predominant method is by finite sums of exponentials in the real-time space [33,34] or rational functions in the Laplace domain or the Fourier space [35–38] to facilitate a fast evaluation. The convergence, stability, and efficiency of these methods have been thoroughly investigated [24,25]. The most extensively studied case is the one-dimensional case. The extensions to high-dimensional cases can be found in Refs. [39–43]; but these methods are often limited only to special geometries of the interior domain. Another classical strategy is the perfectly matched layer (PML) [44], where one first constructs a buffer layer so that the outgoing waves in the computational domain are exactly preserved (perfect matching). The most common approach is to introduce a complex stretching of the spatial coordinate to derive a modified equation in the buffer zone, and then the resulting models are discretized simultaneously in the implementation. The PML has been applied to the nonlinear Schrödinger equation by Zheng [45]. Similarly to the CAP methods, the parameters in the PML method have to be calibrated *a priori*.

In the three-dimensional case, one challenge in implementing the ABCs stems from the fact that the kinetic energy in the Schrödinger equation often needs to be approximated by high-order finite-difference schemes, either to gain sufficient accuracy or to reduce the computational cost by using larger grid size. Therefore, the ABCs that are developed from *continuous* partial differential equations, especially those that are expressed in terms of the normal derivatives of the solution at the boundary [46,47], are difficult to be integrated with the discretization in the computational domain. For instance, due to the large finite-difference stencil, there are several layers of grids at the boundary, where the ABCs need to be applied, which is nontrivial. To overcome this difficulty, we formulate the ABCs based on a semidiscrete approximation of the TDSE obtained from high-order finite-difference schemes in the entire domain. The resulting boundary condition does not need to be further discretized in space. It can be readily implemented. Meanwhile, the time convolution in the corresponding DtN map is formulated and approximated by rational functions in Laplace domain. This approximation reduces the exact DtN map to ordinary differential equations in the time domain, which is much more efficient in practice. We also tackle the important issue that when the domains is of arbitrary geometry, there is no simple representations of the DtN map, e.g., in terms of a pseudodifferential operator [37,48]. In this case, it is expressed as a matrix function which involves the Hamiltonian in the exterior. We will employ the discrete boundary-element method [49] to evaluate the DtN map in the rational interpolation.

We will demonstrate that the first-order ABC obtained from this approach correspond to a CAP method. This offers an interesting connection between the DtN map and an existing method. But the Hamiltonian that represents the absorbing potential is computed from the exact ABC rather than empirically built (e.g., a diagonal matrix). We will also show that the second-order ABC is more general than CAP. In most cases, it is more accurate than the first-order approximation.

This paper is organized as follows: In Sec. II, the solution of the exterior problem, which leads to the exact ABC, is formulated. We approximate the exact boundary condition based on its Laplace transform in Sec. III. We discuss the choices of the interpolation conditions such that the dynamics is stable. In Sec. IV, both 1D and 3D numerical simulations are performed to verify the stability and effectiveness. Further, we test the ABCs on a time-dependent Hartree-Fock (TDHF) model with localized interactions.

II. FORMULATION OF A DISCRETE DTN MAP FOR SCHRÖDINGER-TYPE OF EQUATIONS

This paper is concerned with the time-dependent Schrödinger equations in a domain $\Omega \subset \mathbb{R}^d$,

$$i\frac{\partial}{\partial t}\phi(\boldsymbol{x},t) = \hat{H}\phi(\boldsymbol{x},t), \quad \boldsymbol{x} \in \Omega. \tag{1}$$

Here we have scaled the Planck constant and mass to unity, i is the imaginary unit, and $\phi(\boldsymbol{x},t)$ is the wave function for an electron or nucleon in the d-dimensional quantum system. In general, the Hamiltonian operator can be written as $\hat{H} = -\frac{\nabla^2}{2} + V(\boldsymbol{x},t)$, with V being the total potential of the system. A Schrödinger-like equation can be derived from the exact many-body Schrödinger equation with various mean-field approximations of the many-body wave function, such as the Hartree-Fock approach [50] and the time-dependent density-functional theory [51]. For simplicity, we illustrate the formulation with the simplest model and demonstrate the applications of other Schrödinger-type equations in Sec. IV C.

We suppose that $\Omega_{\rm I}$ is a subdomain of interest in Ω. Rather than solving the Schrödinger equations in the entire domain Ω, we take into account the influence from the surrounding region, here denoted by $\Omega_{\rm II}$ by deriving ABCs at the boundary of $\Omega_{\rm I}$. $\Omega = \Omega_{\rm I} \cup \Omega_{\rm II}$. In the exterior region $\Omega_{\rm II}$, we assume that the operator $\hat{H}$ does not explicitly depend on $\boldsymbol{x}$. More specifically, $V(\boldsymbol{x}) = 0$, or more generally a constant, for any $\boldsymbol{x} \in \Omega_{\rm II}$.

Most ABCs have been formulated in the continuous case [5,27,37,52], which has to be further discretized in order to be combined with the finite-difference or finite-element approximation in the interior of $\Omega_{\rm I}$. For easier implementation, our approach starts directly with a spatially discrete model. Namely, we first consider the semidiscrete approximation of (1) in the entire domain and regard it as a full or exact model. This has been done for the acoustic wave equations in Ref. [53]. But efficient evaluations of the ABCs were not fully discussed there.

Let $\{\boldsymbol{x}_j\}$ be the set of $n_{\rm I}$ grid points with a constant spacing of h in the interior $\Omega_{\rm I}$ and $n_{\rm II}$ grid points in the exterior $\Omega_{\rm II}$. $n_{\rm I} \ll n_{\rm II}$. $n_{\rm II}$ can be infinite. In real-space methods, the Hamiltonian operator in (1) can be approximated by a representation over numerical grids (e.g., Ref. [54]), finite elements (e.g., Ref. [55]), or atom-centered basis set. These spatial approximations reduce the problem to a discrete model in space. Here we take the simplest approach, the finite-difference method, to

demonstrate the formulation of the ABC. To ensure high-order accuracy, these finite-difference methods often employ large stencils. For example, a one-dimensional Laplacian operator, acting on a continuous function $\psi(x,t)$, can be approximated by

$$\frac{\partial^2}{\partial x^2}\psi(x,t) \approx \frac{-\psi_{-2}+16\psi_{-1}-30\psi_0+16\psi_1-\psi_2}{12h^2}.$$

Here $\psi_j(t)=\psi(x+jh,t)$ with h being the grid spacing. In the high-dimensional case, this finite-difference formula can be applied in each direction [56].

Let us introduce some notations to make the derivation more transparent. These notations are largely adopted from domain decomposition methods [57]. To begin with, the indices of the nodal points are sorted as $\boldsymbol{x}_1,\ldots,\boldsymbol{x}_{n_\mathrm{I}} \in \Omega_\mathrm{I}$ and $\boldsymbol{x}_{n_\mathrm{I}+1},\ldots,\boldsymbol{x}_{n_\mathrm{I}+n_\mathrm{II}} \in \Omega_\mathrm{II}$. Due to the discretization in space, the wave functions are written in vectors, and the semidiscrete model can be written in a compact form as follows:

$$\begin{aligned} i\dot{\boldsymbol{\phi}}_\mathrm{I}(t) &= H_{\mathrm{I,I}}\boldsymbol{\phi}_\mathrm{I}(t)+H_{\mathrm{I,II}}\boldsymbol{\phi}_\mathrm{II}(t)\\ i\dot{\boldsymbol{\phi}}_\mathrm{II}(t) &= H_{\mathrm{II,I}}\boldsymbol{\phi}_\mathrm{I}(t)+H_{\mathrm{II,II}}\boldsymbol{\phi}_\mathrm{II}(t), \end{aligned} \tag{2}$$

where $\boldsymbol{\phi}_\mathrm{I}=[\phi(\boldsymbol{x}_k)]_{\boldsymbol{x}_k\in\Omega_\mathrm{I}}$ and $\boldsymbol{\phi}_\mathrm{II}=[\phi(\boldsymbol{x}_k)]_{\boldsymbol{x}_k\in\Omega_\mathrm{II}}$. $\boldsymbol{\phi}_\mathrm{I}\in\mathbb{C}^{n_\mathrm{I}}$ and $\boldsymbol{\phi}_\mathrm{II}\in\mathbb{C}^{n_\mathrm{II}}$; the dot means the derivative with respect to the time t. Following the same partition, the discretization of the Hamiltonian operator H is structured as follows:

$$H=\begin{bmatrix} H_{\mathrm{I,I}} & H_{\mathrm{I,II}} \\ H_{\mathrm{II,I}} & H_{\mathrm{II,II}} \end{bmatrix}. \tag{3}$$

Since the Schrödinger equation (1) has been discretized in space, we use the dot to denote the time derivatives hereafter.

Our goal is to simplify the second equation in (2), while retaining the first equation. $H_{\mathrm{I,I}}$ and $H_{\mathrm{II,II}}$ are, respectively, the discretized Hamiltonian operator in Ω_I and Ω_II. $H_{\mathrm{I,I}}$ can be a nonlinear operator. $H_{\mathrm{I,II}}$ and $H_{\mathrm{II,I}}$ are the off-diagonal blocks representing the coupling between Ω_I and Ω_II. Notice that due to the finite-difference approximation of the kinetic energy term, all these matrices are sparse.

The boundary condition will be expressed in terms of the values of the wave functions near the boundary of Ω_I. To this end, we denote Γ as the boundary of Ω_I, such that

$$\Gamma=\{\boldsymbol{x}_j\in\Omega_\mathrm{I}|\text{ if there exists }\boldsymbol{x}_k\in\Omega_\mathrm{II}\text{ such that }H_{jk}\neq 0\}. \tag{4}$$

The width of Γ depends on the width of the finite-difference stencil. We define $\boldsymbol{\phi}_\Gamma\in\mathbb{C}^{n_\Gamma}$ as a vector formed by all $\boldsymbol{\phi}_j$ for $\boldsymbol{x}_j\in\Gamma$, where n_Γ is the number of grid points in Γ. The vector $\boldsymbol{\phi}_\mathrm{I}$ can be reordered so that the first n_Γ components are associated with the grid points in Γ, i.e.,

$$\boldsymbol{\phi}_\mathrm{I}=\begin{bmatrix}\boldsymbol{\phi}_\Gamma\\ \boldsymbol{\phi}_{\mathrm{I}\setminus\Gamma}\end{bmatrix}. \tag{5}$$

The boundary region Γ is defined in such a way that there is no direct coupling between the points in the interior of Ω_I and those in Ω_II. This is reflected in the off-diagonal block of the Hamiltonian,

$$H_{\mathrm{II,I}}=[H_{\mathrm{II},\Gamma}\;\; H_{\mathrm{II},\mathrm{I}\setminus\Gamma}]=[H_{\mathrm{II},\Gamma}\;\; 0]. \tag{6}$$

In general, this procedure can be carried out by defining a restriction operator E to extract the components of a function that correspond to grid points at the boundary Γ from a function defined in Ω_I. Namely,

$$\boldsymbol{\phi}_\Gamma = E\boldsymbol{\phi}_\mathrm{I}. \tag{7}$$

With the reordering in (5), the matrix $E\in\mathbb{R}^{n_\Gamma\times n_\mathrm{II}}$ can be explicitly expressed as $E=[I_{n_\Gamma}\;\; 0]$. Further, (6) can now be simply written as $H_{\mathrm{II},\Gamma}=H_{\mathrm{II,I}}E^T$. Since $EE^T=I_{n_\Gamma}$, we also have

$$H_{\mathrm{I,II}}=E^TH_{\Gamma,\mathrm{II}}. \tag{8}$$

We are now set to formulate the ABC. We first consider the influence of the wave functions in Ω_II on the wave functions in Ω_I, and we define

$$\boldsymbol{f}_\Gamma = H_{\Gamma,\mathrm{II}}\boldsymbol{\phi}_\mathrm{II}. \tag{9}$$

Then the first equation reads

$$\dot{\boldsymbol{\phi}}_\mathrm{I}(t) = -iH_{\mathrm{I,I}}\boldsymbol{\phi}_\mathrm{I}(t)-iE^T\boldsymbol{f}_\Gamma(t). \tag{10}$$

Here the dot denotes the derivative with respect to the time variable t.

At this point, we observe that what is needed to compute $\boldsymbol{\phi}_\mathrm{I}$ in time is $\boldsymbol{f}_\Gamma(t)$. For this purpose, let us take the Laplace transform of the second equation in (2). Due to the assumption that $\Phi_\mathrm{II}(0)=0$, one has

$$is\boldsymbol{\Phi}_\mathrm{II}(s) = H_{\mathrm{II,II}}\boldsymbol{\Phi}_\mathrm{II}(s)+H_{\mathrm{II,I}}\boldsymbol{\Phi}_\mathrm{I}(s), \tag{11}$$

where $\boldsymbol{\Phi}_\mathrm{II}(s)=\mathcal{L}\{\boldsymbol{\phi}_\mathrm{II}\}(s)$ and $\boldsymbol{\Phi}_\mathrm{I}(s)=\mathcal{L}\{\boldsymbol{\phi}_\mathrm{I}\}(s)$. By defining $\widetilde{H}_{\mathrm{II,II}}(s)=H_{\mathrm{II,II}}-isI$, Eq. (11) simply reads

$$\widetilde{H}_{\mathrm{II,II}}(s)\boldsymbol{\Phi}_\mathrm{II}(s) = -H_{\mathrm{II,I}}\boldsymbol{\Phi}_\mathrm{I}(s). \tag{12}$$

Formally, its solution can be expressed as

$$\boldsymbol{\Phi}_\mathrm{II}(s) = -\widetilde{H}^{-1}_{\mathrm{II,II}}H_{\mathrm{II,I}}\boldsymbol{\Phi}_\mathrm{I}(s). \tag{13}$$

Due to the locality of $H_{\mathrm{II,II}}$, the right-hand side of (13) can be further reduced. Notice that

$$H_{\mathrm{II,I}}\boldsymbol{\Phi}_\mathrm{I} = H_{\mathrm{II},\Gamma}E\boldsymbol{\Phi}_\mathrm{I} = H_{\mathrm{II},\Gamma}\boldsymbol{\Phi}_\Gamma.$$

The first step is from the identity (6), and the second step used (7). This simplifies the solution to

$$\boldsymbol{\Phi}_\mathrm{II}(s) = -\widetilde{H}^{-1}_{\mathrm{II,II}}H_{\mathrm{II},\Gamma}\boldsymbol{\Phi}_\Gamma(s). \tag{14}$$

Since $H_{\mathrm{II,II}}$ is a $n_\mathrm{II}\times n_\mathrm{II}$ matrix, it is in general impractical to solve the linear system (14) numerically. However, the main observation from (10) is that we only need $\boldsymbol{f}_\Gamma$ to keep the computation in Ω_I. We let $\boldsymbol{F}_\Gamma$ be the Laplace transform of $\boldsymbol{f}_\Gamma$. By left-multiplying the equation above by $H_{\Gamma,\mathrm{II}}$, we obtain

$$\boldsymbol{F}_\Gamma(s) = K(s)\boldsymbol{\Phi}_\Gamma(s). \tag{15}$$

The matrix-valued function $K(s):\mathbb{R}\to\Omega_\Gamma\times\Omega_\Gamma$, which will play a key role in the numerical approximation, is given by

$$K(s) = -H_{\Gamma,\mathrm{II}}\widetilde{H}^{-1}_{\mathrm{II,II}}(s)H_{\mathrm{II},\Gamma} = -H_{\Gamma,\mathrm{II}}[H_{\mathrm{II,II}}-isI]^{-1}H_{\mathrm{II},\Gamma}. \tag{16}$$

The mapping $K(s)$ is precisely the DtN map of the problem (2) in the Laplace domain. Although $K(s)$ still involves the inverse of a large matrix, it is much easier to compute than (14) due to the fact that only a small number of entries are needed. This is known as selected inversion [58]. The

detailed solution to this problem, which involves a discrete boundary element method, will be discussed in Sec. III and Appendix A.

In the time domain, the DtN map becomes a time convolution,

$$f_\Gamma(t) = \int_0^t \kappa(t-\tau)\boldsymbol{\phi}_\Gamma(\tau)d\tau. \tag{17}$$

With the DtN map, we incorporate (17) into (10), and we arrive at a reduced problem (2),

$$\dot{\boldsymbol{\phi}}_{\mathrm{I}}(t) = -iH_{\mathrm{I,I}}\boldsymbol{\phi}_{\mathrm{I}}(t) - iE^T\int_0^t \kappa(t-\tau)E\boldsymbol{\phi}_{\mathrm{I}}(\tau)d\tau, \tag{18}$$

where $\kappa(t)$ is the real-time kernel function which corresponds to $K(s)$ in the Laplace domain.

The main difficulties in implementing the transparent boundary condition (17) are as follows: (i) There is no analytical expression for $K(s)$ or $\kappa(t)$ in general, other than the formula (16) in terms of a large-dimensional matrix, in which case it is expensive to evaluate $K(s)$ or $\kappa(t)$ repeatedly. (ii) The direct evaluation of the time-convolution integral adds up quickly to the computational cost: Since the kernel function $\kappa(t)$ does not have compact support in time, long-time integration is required to evaluate the exact boundary condition.

In light of these concerns, we will introduce further approximations in the next section.

Remark 2.1. Our procedure for reducing the problem is reminiscent of reduced-order modeling [59,60]. More specifically, the quantity $\boldsymbol{f}_\Gamma$ can be viewed as the low-dimensional output, and $\boldsymbol{\phi}_\Gamma$ corresponds to the control quantity. In the reduced-order literature, it is sometimes convenient to write (11) into the alternative form

$$\begin{aligned} &i(s-s_0)(H_{\mathrm{II,II}} - is_0 I)^{-1}\boldsymbol{\Phi}_{\mathrm{II}}(s) \\ &\quad = \boldsymbol{\Phi}_{\mathrm{II}}(s) + (H_{\mathrm{II,II}} - is_0 I)^{-1}H_{\mathrm{II,I}}\boldsymbol{\Phi}_{\mathrm{I}}(s), \end{aligned} \tag{19}$$

where $s_0 \in \mathbb{C}$ is a preselected scalar. In this case, the kernel function becomes

$$\begin{aligned} K(s) = &-H_{\Gamma,\mathrm{II}}[I - i(s-s_0)(H_{\mathrm{II,II}} - is_0 I)^{-1}]^{-1} \\ &\times (H_{\mathrm{II,II}} - is_0 I)^{-1}H_{\mathrm{II},\Gamma}. \end{aligned} \tag{20}$$

If we denote $\mathcal{A} = i(H_{\mathrm{II,II}} - is_0)^{-1}$ and $C = (H_{\mathrm{II,II}} - is_0 I)^{-1}H_{\mathrm{II},\Gamma}$, then the Taylor expansion of the kernel function $K(s)$ around $s = s_0$ reads

$$\begin{aligned} K(s) = &-H_{\Gamma,\mathrm{II}}[C + \mathcal{A}C(s-s_0) + \mathcal{A}^2C(s-s_0)^2 \\ &+ \mathcal{A}^3C(s-s_0)^3 + \cdots]. \end{aligned} \tag{21}$$

The coefficients (moments) in the expansion are $M_0 = -H_{\Gamma,\mathrm{II}}C$, $M_1 = -H_{\Gamma,\mathrm{II}}\mathcal{A}C$, $M_2 = -H_{\Gamma,\mathrm{II}}\mathcal{A}^2C$, etc. One way to approximate the kernel function $K(s)$ is by rational functions with the same moments, which is known as *moment matching* [59,61]. One may also notice that (21) is connected to a Krylov subspace $\mathcal{K}(\mathcal{A}, C)$. However, for the problem considered here, the higher powers of $\mathcal{A}$ are much more difficult to compute.

III. APPROXIMATION OF THE DISCRETE DTN MAP

Consider the following rational functions:

$$\begin{aligned} R_{m,m}(s) = &(s^m - s^{m-1}B_0 - \cdots - B_{m-1})^{-1} \\ &\times (s^{m-1}A_0 + \cdots + A_{m-1}). \end{aligned} \tag{22}$$

$A_0, \ldots, A_{m-1}$ and $B_0, \ldots, B_{m-1}$ are $n_\Gamma \times n_\Gamma$ matrices to be determined. Here the integer $m \geqslant 0$ will be referred to as the *order* of the approximation.

The rational approximation reduces the DtN map in the Laplace domain to

$$\boldsymbol{F}_\Gamma(s) = R_{m,m}(s)\boldsymbol{\Phi}_\Gamma(s). \tag{23}$$

One advantage of the rational approximation is that in the time domain, the dynamics can be represented by an ordinary differential equation (ODE),

$$\begin{aligned} \boldsymbol{f}_\Gamma^{(m)} = &B_0\boldsymbol{f}_\Gamma^{(m-1)} + \cdots + B_{m-1}\boldsymbol{f}_\Gamma \\ &+ A_0\boldsymbol{\phi}_\Gamma^{(m-1)} + \cdots + A_{m-1}\boldsymbol{\phi}_\Gamma, \end{aligned} \tag{24}$$

assuming appropriate initial conditions. The superscript (m) denotes the mth derivative. Now, the nonlocal time convolution in the DtN map (Eq. (18)) is replaced by a linear ODE system, which is much more efficient in practical implementations. The reduced model [Eq. (2)] is replaced by

$$\begin{aligned} \frac{\partial}{\partial t}\boldsymbol{\phi}_{\mathrm{I}}(t) = &-iH_{\mathrm{I,I}}\boldsymbol{\phi}_{\mathrm{I}}(t) - iH_{\mathrm{I,II}}\boldsymbol{\phi}_{\mathrm{II}}(t) \\ \boldsymbol{f}_\Gamma^{(m)} = &B_0\boldsymbol{f}_\Gamma^{(m-1)} + \cdots + B_{m-1}\boldsymbol{f}_\Gamma + A_0\boldsymbol{\phi}_\Gamma^{(m-1)} \\ &+ \cdots + A_{m-1}\boldsymbol{\phi}_\Gamma. \end{aligned} \tag{25}$$

The remaining question is how to determine the coefficients A_i and B_i. This is done by interpolation. Namely we match $R_{m,m}(s)$ to $K(s)$ at certain points. In principle we need $2m$ points of $(s_i, K(s_i))$ to determine these coefficients. In general, one may hope that the accuracy would improve as the number of interpolation points increases. However, a more subtle issue is the stability of the system (25). The semidiscrete models are quite similar to molecular dynamics models, for which the stability of ABCs has been analyzed in Ref. [62]. In particular, the Lyapunov functional approach is quite useful. In this paper, we will present the guaranteed stability of the zeroth-order ($m = 0$) and first-order approximation ($m = 1$). We did not find a simple proof of stability for higher-order approximations, and we will resort to our numerical simulations to examine the stability property.

Remark 3.1. We did not pursue a one-point Padé approximation, or the Krylov subspace projections, which has been overwhelmingly successful in reduced-order modeling [59]. The main reason is that in our case, a selected inversion of $(H_{\mathrm{II,II}} - is_0)$ can be done very efficiently, but the higher-order inverse is very difficult.

A. Zeroth-order approximation

For the zeroth-order approximation, $R_{0,0}$ becomes a constant matrix, here denoted by M. We restrict M to be a Hermitian matrix. The corresponding dynamics is

$$\dot{\boldsymbol{\phi}}_{\mathrm{I}}(t) = -iH_{\mathrm{I,I}}\boldsymbol{\phi}_{\mathrm{I}}(t) - iE^TME\boldsymbol{\phi}_{\mathrm{I}}(t). \tag{26}$$

Theorem 3.1. (Stability condition of the zero-order approximation). The dynamics [Eq. (26)] is stable if M is chosen as $K(s_0)$ for an arbitrary positive value of s_0 ($s_0 \geqslant 0$).

Proof. We define a Lyapunov functional as

$$W(t) = \boldsymbol{\phi}_{\mathrm{I}}^*(t)\boldsymbol{\phi}_{\mathrm{I}}(t). \tag{27}$$

We examine the derivative of the Lyapunov functional,

$$\begin{aligned}\frac{dW}{dt} &= \frac{d}{dt}\boldsymbol{\phi}_{\mathrm{I}}^*\boldsymbol{\phi}_{\mathrm{I}} + \boldsymbol{\phi}_{\mathrm{I}}^*\frac{d}{dt}\boldsymbol{\phi}_{\mathrm{I}} \\ &= i(\boldsymbol{\phi}_{\mathrm{I}}^* H_{\mathrm{I,I}} + \boldsymbol{\phi}_{\Gamma}^* M^* E)\boldsymbol{\phi}_{\mathrm{I}} - i\boldsymbol{\phi}_{\mathrm{I}}^*(H_{\mathrm{I,I}}\boldsymbol{\phi}_{\mathrm{I}} + E^T M\boldsymbol{\phi}_{\Gamma}) \\ &= i\boldsymbol{\phi}_{\Gamma}^*(M^* - M)\boldsymbol{\phi}_{\Gamma}. \end{aligned} \tag{28}$$

This indicates that if M has a negative definite imaginary part, then $\frac{dW}{dt} \leqslant 0$. To verify this, we note that since $-H_{\mathrm{I,II}}[H_{\mathrm{II,II}} - is_0 I]^{-1}H_{\mathrm{II,I}} = -H_{\mathrm{I,II}}(H_{\mathrm{II,II}}^2 + s_0^2 I)^{-1}(H_{\mathrm{II,II}} + is_0 I)H_{\mathrm{II,I}}$, $K(s_0)$ always has a negative imaginary part as long as s_0 is real and positive. Therefore, the dynamics (26) is stable. ■

This shows that the stability does not depend on the choice of the interpolation point.

Remark 3.2. The stability analysis also reveals that the additional term in (26) has an imaginary part that acts as a CAP. However, unlike the commonly used CAP methods [13–15], this term is derived from the DtN map, and it is dependent of the mesh size, finite-difference formulas, as well as the geometry of the domain. Further, the higher-order approximations of the DtN map, which will be presented next, provide a more general form that goes beyond the CAP methods.

B. First-order approximation

For the first-order approximation, we use the rational function $R_{1,1} = (sI - B)^{-1}A$ to approximate the DtN map. The first-order approximated dynamics is

$$\begin{aligned}\dot{\boldsymbol{\phi}}_{\mathrm{I}}(t) &= -iH_{\mathrm{I,I}}\boldsymbol{\phi}_{\mathrm{I}}(t) - iE^T\boldsymbol{f}_{\Gamma}(t) \\ \dot{\boldsymbol{f}}_{\Gamma}(t) &= B\boldsymbol{f}_{\Gamma}(t) + AE\boldsymbol{\phi}_{\mathrm{I}}(t). \end{aligned} \tag{29}$$

To verify the stability, we introduce a Lyapunov functional,

$$W(t) = \boldsymbol{\phi}_{\mathrm{I}}^*(t)\boldsymbol{\phi}_{\mathrm{I}}(t) + \boldsymbol{f}_{\Gamma}^*(t)Q\boldsymbol{f}_{\Gamma}(t), \tag{30}$$

where Q is a positive definite matrix to be determined. The derivative of the above Lyapunov functional is

$$\begin{aligned}\frac{dW}{dt} &= \frac{d}{dt}\boldsymbol{\phi}_{\mathrm{I}}^*\boldsymbol{\phi}_{\mathrm{I}} + \boldsymbol{\phi}_{\mathrm{I}}^*\frac{d}{dt}\boldsymbol{\phi}_{\mathrm{I}} + \frac{d}{dt}\boldsymbol{f}_{\Gamma}^*Q\boldsymbol{f}_{\Gamma} + \boldsymbol{f}_{\Gamma}^*Q\frac{d}{dt}\boldsymbol{f}_{\Gamma} \\ &= (i\boldsymbol{\phi}_{\mathrm{I}}^* H_{\mathrm{I,I}} + i\boldsymbol{f}_{\Gamma}^* E)\boldsymbol{\phi}_{\mathrm{I}} + \boldsymbol{\phi}_{\mathrm{I}}^*(-iH_{\mathrm{I,I}}\boldsymbol{\phi}_{\mathrm{I}} - iE^T\boldsymbol{f}_{\Gamma}) \\ &\quad + (\boldsymbol{f}_{\Gamma}^* B^* + \boldsymbol{\phi}_{\mathrm{I}}^* E^T A^*)Q\boldsymbol{f}_{\Gamma} + \boldsymbol{f}_{\Gamma}^* Q(B\boldsymbol{f}_{\Gamma} + AE\boldsymbol{\phi}_{\mathrm{I}}) \\ &= \boldsymbol{f}_{\Gamma}^*(iI + QA)E\boldsymbol{\phi}_{\mathrm{I}} + \boldsymbol{\phi}_{\mathrm{I}}^* E^T(-iI + A^*Q)\boldsymbol{f}_{\Gamma} \\ &\quad + \boldsymbol{f}_{\Gamma}^*(B^*Q + QB)\boldsymbol{f}_{\Gamma}. \end{aligned} \tag{31}$$

At this point, we observe that if $iI + QA = 0$, and $B^*Q + QB$ has negative definite real part, then the dynamics (29) is stable. The following theorem provides a guideline for the choice of the interpolation points to ensure stability.

Theorem 3.2 (Stability condition of the first-order approximation). The dynamics [Eq. (29)] is stable if the coefficients A and B are determined by the interpolations $\lim_{\lambda\to 0}\frac{d}{d\lambda}R'_{1,1} = \lim_{\lambda\to 0}\frac{d}{d\lambda}K$, where $\lambda = s^{-1}$, and $R_{1,1}(s_1) = K(s_1)$, where s_1 is a any positive real number.

Proof. From

$$\lim_{\lambda\to 0}\frac{d}{d\lambda}R_{1,1} = \lim_{\lambda\to 0}\frac{d}{d\lambda}K,$$

we have

$$A = -iH_{\Gamma,\mathrm{II}}H_{\mathrm{II},\Gamma}.$$

Now we pick $Q = (H_{\Gamma,\mathrm{II}}H_{\mathrm{II},\Gamma})^{-1}$. Q is symmetric positive definite. The Lyapunov functional [Eq. (30)] is thus positive definite. Let us denote $K_1 = K(s_1)$. When $R_{1,1}(s_1) = K(s_1)$, we have

$$B = s_1 I - AK_1^{-1}.$$

Hence, $QB = -is_1A^{-1} + iK_1^{-1}$. Next, we show that QB has a negative definite imaginary part. We start with

$$\begin{aligned}QB + B^*Q &= 2s_1(H_{\Gamma,\mathrm{II}}H_{\mathrm{II},\Gamma})^{-1} + i(K_1^{-1} - (K_1^*)^{-1}), \\ &= 2s_1(H_{\Gamma,\mathrm{II}}H_{\mathrm{II},\Gamma})^{-1} + i(K_1^*)^{-1}(K_1^* - K_1)K_1^{-1}. \end{aligned} \tag{32}$$

To continue, we denote $P_1 = (H_{\mathrm{II,II}} - is_1 I)^{-1}H_{\mathrm{II},\Gamma}$. As a result, $K_1 = -H_{\mathrm{II},\Gamma}P_1$, and

$$\begin{aligned}K_1^* - K_1 &= -H_{\Gamma,\mathrm{II}}(H_{\mathrm{II,II}} + is_1 I)^{-1}H_{\mathrm{II},\Gamma} \\ &\quad + H_{\Gamma,\mathrm{II}}(H_{\mathrm{II,II}} - is_1 I)^{-1}H_{\mathrm{II},\Gamma}, \\ &= 2is_1 P_1^* P_1. \end{aligned} \tag{33}$$

Therefore we have

$$\begin{aligned}QB + B^*Q &= 2s_1(K_1^*)^{-1}[K_1^*(H_{\Gamma,\mathrm{II}}H_{\mathrm{II},\Gamma})^{-1}K_1 - P_1^*P_1]K_1^{-1} \\ &= 2s_1(K_1^*)^{-1}[P_1^*H_{\Gamma,\mathrm{II}}(H_{\Gamma,\mathrm{II}}H_{\mathrm{II},\Gamma})^{-1} \\ &\quad \times H_{\mathrm{II},\Gamma}P_1 - P_1^*P_1]K_1^{-1}, \\ &= 2s_1(K_1^*)^{-1}P_1^*[H_{\mathrm{II},\Gamma}(H_{\Gamma,\mathrm{II}}H_{\mathrm{II},\Gamma})^{-1}H_{\Gamma,\mathrm{II}} - I]P_1K_1^{-1}. \end{aligned} \tag{34}$$

Since $H_{\mathrm{II},\Gamma}(H_{\Gamma,\mathrm{II}}H_{\mathrm{II},\Gamma})^{-1}H_{\Gamma,\mathrm{II}}$ is an orthogonal projection matrix, $H_{\mathrm{II},\Gamma}(H_{\Gamma,\mathrm{II}}H_{\mathrm{II},\Gamma})^{-1}H_{\Gamma,\mathrm{II}} - I$ is symmetric negative semidefinite. As a result, $QB + B^*Q$ is negative semidefinite. Therefore, the dynamics [Eq. (29)] is stable.

The interpolation scheme suggested in the theorem involves an interpolation point $s_1 > 0$ and another point toward $s_2 \to +\infty$. Our numerical tests indicate that the approximation is still stable when s_2 is finite.

C. Second-order approximation

The rational function approximation can be extended to higher order. We briefly describe the second-order approximation here, in which case the DtN map is approximated by $R_{2,2} = (s^2I - sB_1 - B_0)^{-1}(sA_1 + A_0)$, and the dynamics augmented with this ABC is given by

$$\begin{aligned}\dot{\boldsymbol{\phi}}_{\mathrm{I}}(t) &= -iH_{\mathrm{I,I}}\boldsymbol{\phi}_{\mathrm{I}}(t) - iE^T\boldsymbol{f}_{\Gamma}(t) \\ \ddot{\boldsymbol{f}}_{\Gamma}(t) &= B_1\dot{\boldsymbol{f}}_{\Gamma}(t) + B_0\boldsymbol{f}_{\Gamma}(t) + A_1E\dot{\boldsymbol{\phi}}_{\mathrm{I}}(t) + A_0E\boldsymbol{\phi}_{\mathrm{I}}(t). \end{aligned} \tag{35}$$

In the above equation, double dots denote the second derivative with respect to the time. We have not found a simple proof that provides the stability condition of the dynamics (35) in

terms of the interpolation points. The stability will thus be demonstrated by numerical tests in Sec. IV.

IV. APPLICATIONS AND NUMERICAL EXPERIMENTS

In this section, we test the ABCs with three examples. For each model, the details regarding the numerical tests are respectively discussed in Sec. IV A, Sec. IV B, and Sec. IV C. The three problems are briefly summarized as follows:

(i) A 1D time-dependent Schrödinger equation extensively used as a test example in the literature [24], although our main emphasis is on Schrödinger equation in $\mathbb{R}^3$. The system is a 1D free electron,

$$i\frac{\partial}{\partial t}\psi(x,t) = \widehat{H}\psi(x,t), \widehat{H} = -\frac{\partial_x^2}{2} \text{ in } \mathbb{R}, \tag{36}$$

with the initial condition $\psi^0(x) = \exp[-(x-x_c)^2 + ik_0(x-x_c)]$.

(ii) A 3D time-dependent Schrödinger equation considered in Ref. [40]:

$$i\frac{\partial}{\partial t}\psi(\boldsymbol{x},t) = \widehat{H}\psi(\boldsymbol{x},t), \widehat{H} = -\frac{\nabla^2}{2} \text{ in } \mathbb{R}^3, \tag{37}$$

with the initial condition $\psi^0(x) = \exp(-x_1^2 - x_2^2 - x_3^2 + ik_0x_1)$.

(iii) A 3D time-dependent Hartree-Fock model [63]:

$$i\frac{\partial}{\partial t}\varphi_j(\boldsymbol{x},t) = \widehat{H}\varphi_j(\boldsymbol{x},t) \text{ in } \mathbb{R}^3, \text{ for } j = 1,\ldots,A, \tag{38}$$

with the initial condition φ_j^0 determined from the ground state. The form of $\widehat{H}$ is given by (49) later in this section. The 3D TDHF model is a system of nonlinear 3D time-dependent Schrödinger equations. The Hamiltonian $\hat{H}$ depends on the one-particle wave functions.

Integrators. In general, numerical integrators can be formulated as [64]

$$\phi^{(n+1)} = U\phi^{(n)}, \tag{39}$$

where U is the operator that mimics the time evolution operator. For linear problems with time-independent potential, the exact operator is a matrix exponential,

$$U_E(t,t') = \exp[-i\Delta t H(t')]. \tag{40}$$

One widely used method is the Crank-Nicholson scheme,

$$U_{\text{CN}} = (1 + i\Delta t/2H)^{-1}(1 - i\Delta t/2H). \tag{41}$$

For the 3D case, it is often impractical to perform the matrix inversion in the Crank-Nicholson scheme. In time dependent density functional theory [1,64,65], one classical method is the Taylor expansion of the exact integrator,

$$U_5 = I - iH\Delta t - \tfrac{1}{2}H^2(\Delta t)^2 + \tfrac{1}{6}H^3(\Delta t)^3 - i\tfrac{1}{24}H^4(\Delta t)^4. \tag{42}$$

Clearly, the operator U_5 is not unitary. However, we will choose Δt to be sufficiently small, in which case this integrator is stable and accurate [10]. This allows us to focus more on the performance of various ABCs.

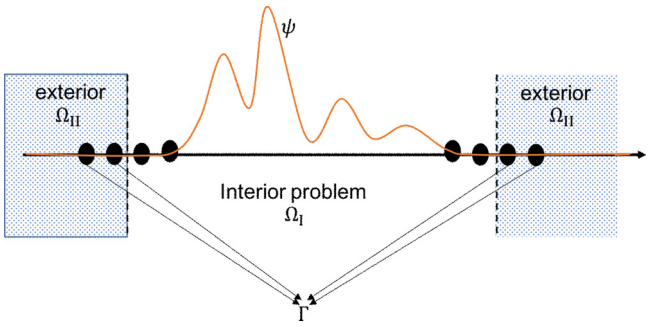

FIG. 1. An illustration of the model reduction for one-dimensional Schrödinger equation. ψ is the wave function, initially supported in the computational domain Ω_{I}.

A. The 1D time-dependent Schrödinger equation

In the first test, we look at a 1D quantum system. The setting of the problem is illustrated in Fig. 1.

The analytical solution of Eq. (36) can be explicitly written as

$$\psi^{\text{ex}}(x,t) = \sqrt{\frac{i}{i-2t}}\exp\left[\frac{-k_0(x-x_c) + k_0^2 t - i(x-x_c)^2}{i-2t}\right], \tag{43}$$

assuming the initial condition

$$\psi^0(x) = \exp[ik_0(x-x_c) - (x-x_c)^2]. \tag{44}$$

The initial condition ψ^0 is localized around x_c, which is the center of the wave packet. k_0 is the wave number. In this test, we set $k_0 = 5$ and $x_c = -6$. The exact solution, ψ^{ex}, propagates to the right when $k_0 > 0$. Therefore, we only need to implement an ABC on the right boundary. A Dirichlet boundary condition will be imposed on the left.

In our simulations, we pick the interior region to be $\Omega_{\text{I}} = [-12, 3]$ and the exterior domain is $\Omega_{\text{II}} = (\infty, -12) \cup (3, \infty)$. The Laplacian operator is discretized by the five-point scheme with grid spacing of $h = 0.01$.

The evaluation of the DtN map is discussed in our previous work [66] using the discrete Green's function. The details of 1D lattice Green's function will be discussed in the Appendix B. We select $s = 20$ for the zeroth-order approximation, two points $s = 10$, and 20 for the first-order approximation and four interpolation points, $s = 10$, 11, 20, 21, for the second-order approximation. The zeroth-order approximation corresponds to a complex absorbing potential over two grid points at the boundary. But we point out that in practice, the latter method can be applied to a much larger buffer region. In accordance with the width of the finite-difference stencil, four and eight extra variables are introduced in the first-order and second-order approximations, respectively.

The solution computed with the Dirichlet boundary condition is completely reflected back into the interior region when the wave function propagates to the boundary (Fig. 2). The zeroth-order approximation causes some reflection when the wave packet first arrives at the boundary, but most of the reflection is eliminated eventually. The first-order ABC qualitatively captures the transient profile of the exact solution, with some errors when the wave reaches the boundary. The second-order ABC provides a much more accurate solution.

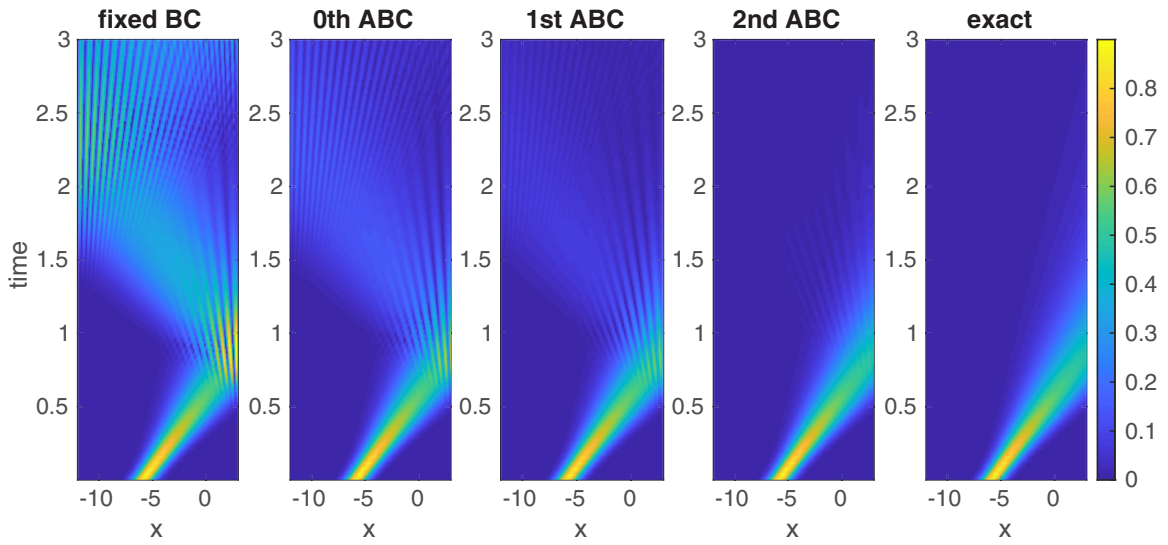

FIG. 2. The solutions computed using fixed boundary condition, zeroth-order, first-order, and second-order ABCs compared with the exact solution.

The solution with ABCs is systematically improved as the order of the approximation increases. In Fig. 3, the total electron number (L_2 norm of the wave function in the computational domain) is presented. Before $t = 0.5$, the electron number in four cases is the same. The norm of the wave function does not decay with the fixed boundary condition since all the wave function are reflected. The electron number by the first-order ABC decays slower than the exact one. In the second-order approximation, the maximum error in the L_2 norm over time is less than 3×10^{-3}.

In the proposed ABCs, one can either improve the order of ABCs or optimize the interpolation points. In most absorbing techniques, the adjustable parameters are the width of the buffer region or the absorbing strength. It is generally difficult to quantitatively compare the absorbing properties of these methods. As a qualitative comparison, we implemented the following CAP [14]:

$$W(x) = \begin{cases} (x+16)^2, & -16 < x < -12 \\ (x-7)^2, & 3 < x < 7, \\ 0, & \text{otherwise} \end{cases} \tag{45}$$

in the 1D model. The size of the buffer region is fixed in our simulations. This leads to the effective Hamiltonian $H^{\text{eff}}(\eta) = H - i\eta W$ on the interval $[-16, 7]$, where η is the CAP strength. The CAP varies from 0.01 to 10 (Fig. 3). When η is smaller than 0.1, we still observed the reflection from the buffer region. When $\eta = 1$, we observed the decent accuracy (98%). As a comparison, this is also achieved by the proposed first-order approximation without optimizing the interpolation conditions and without introducing a buffer region.

B. A 3D time-dependent Schrödinger equation

In this section, we will test the absorbing boundary conditions for the 3D Schrödinger equation for a free electron. We restrict the computational domain in a box $[-1.5, 1.5] \times [-1.5, 1.5] \times [-1.5, 1.5]$. The 3D Laplace operator is approximated by the 7-point finite-difference scheme in each direction with uniform grid spacing of $h = 0.1$. Consequently, there are 31 interior points and 6 exterior points in each axis direction. For each interpolation point, the DtN map $K(t)$ is a 14 166 × 14 166 dense matrix. The coefficients of the

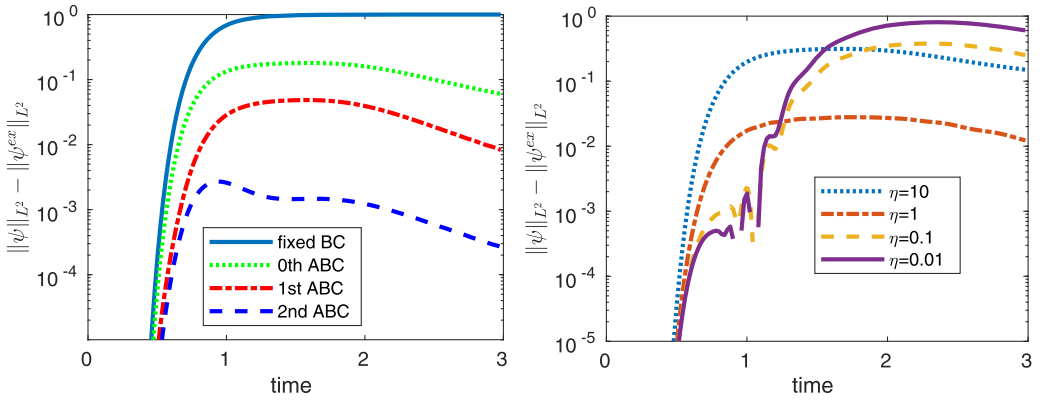

FIG. 3. Comparison of the total electron density in Ω_I with different ABCs (left). Comparison of the total electron density in Ω_I with different complex absorbing potential strength (right).

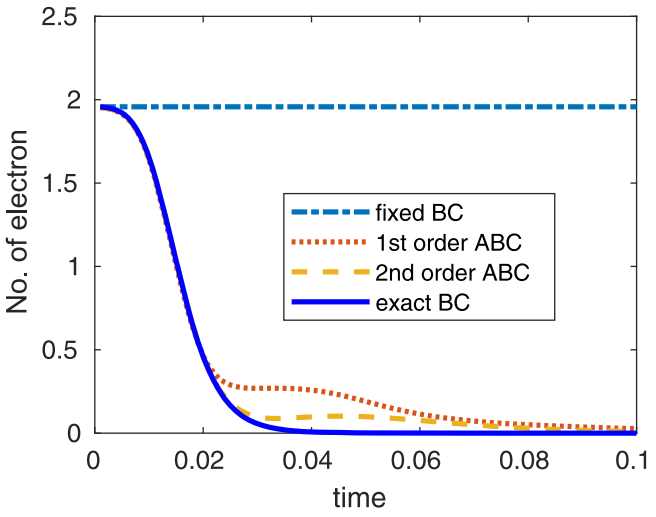

FIG. 4. The number of electrons as a function of time.

first-order ABC are computed by interpolation of $s = 1, 2$. Four interpolation points $s = 1, 2, 3, 10$ are used for the second-order ABC.

Similarly to the 1D case, we still can construct the analytical solution of Eq. (37),

$$\psi^{ex} = \left(\frac{i}{i-2t}\right)^{\frac{3}{2}} \exp\left[\frac{-i\left(x_1^2+x_2^2+x_3^2\right)-k_0x_1+\frac{1}{2}k_0^2t}{i-2t}\right] \tag{46}$$

with $k_0 = 5$. One should notice that the difference between the analytical solution and the exact solution of the discrete model might not be small due to the large grid spacing. Therefore, we will only use the analytical solution as a reference for qualitative comparisons.

For the time integration, the step size is chosen as $\Delta t = 0.001$. In the first test, we observe how the total electron density in Ω_I changes in time (Fig. 4). The number of electrons is almost a constant when we fix the wave function at the boundary (Dirichlet boundary condition). If we impose the ABC on the system, then the number of electrons will decrease after the wave function propagates to the boundary. With the first-order ABC, about 20% of the wave function in magnitude is reflected. Much more reflections are reduced by the second-order ABC. Over a longer time period, such reflections occur multiple times for both the first-order ABC and the second-order ABC. After that, almost all the electrons are emitted out of the box.

The top view of surface plots of solutions of 3D time-dependent Schrödinger equation with different boundary conditions are shown in Fig. 5. The fixed boundary condition leads to significant reflections. From $t = 0.011$, it does not provide any significant results. These errors are reduced by the absorbing boundary conditions. Some reflections are still observed in the first-order approximation. The reflections in the second-order ABC are almost negligible. This experiment also shows that the proposed ABCs is not sensitive to the presence of corners and edges along the boundary. Even though the wave function propagates to the corners, no significant reflection is observed around the corners.

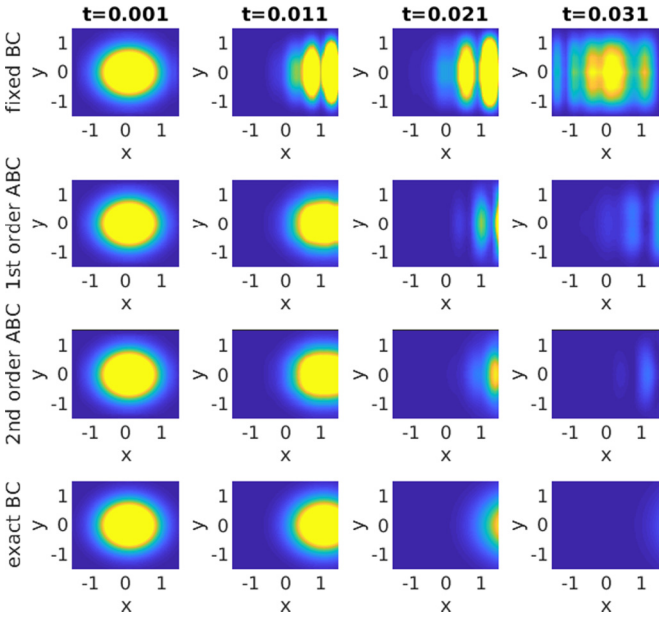

FIG. 5. Projection of the 3D electron density on x-y plane. Time-dependent Schrödinger equation with the fixed boundary condition (first row), the first-order ABC (second row), the second-order ABC (third row), and the exact solution (last row). The color indicated the electron density.

C. 3D time-dependent Hartree-Fock model with localized interactions

The Hartree-Fock equation for a nucleon system can be formulated from the many-body system by approximating the many-body wave function with the Slater determinant and applying the variational principle of the Skyrme functional [63,67,68] with respect to the wave function. The direct procedure yields the coupled TDHF equations with localized interactions,

$$i\hbar\frac{\partial}{\partial t}\varphi_j(\boldsymbol{r},t) = H(t,\rho)\varphi_j(\boldsymbol{r},t), \quad j = 1,\ldots,A, \tag{47}$$

where H is the time-dependent one-body HF Hamiltonian. The one-body Hamiltonian depends on the nucleon density, given by

$$\rho(\boldsymbol{r},t) = \sum_{j=1}^{A}|\varphi_j(\boldsymbol{r},t)|^2. \tag{48}$$

The one-body HF Hamiltonian can be explicitly written as

$$H = -\frac{\hbar^2}{2m}\Delta + \frac{3}{4}t_0\rho + \frac{3}{16}t_3\rho^2 + W_y + W_C. \tag{49}$$

Here t_0 and t_3 are the coefficients of the Skyrme interactions [63,67,68]. Among the five terms in the one-body Hamiltonian, the first term is from the kinetic energy. The following two terms are the expectation value of the zero-range density-dependent two-body effective interaction. Furthermore, W_y is the Yukawa potential,

$$W_y(\boldsymbol{r}) = V_0\int d\boldsymbol{r}\frac{\exp-|\boldsymbol{r}-\boldsymbol{r}'|/a}{|\boldsymbol{r}-\boldsymbol{r}'|/a}\rho(\boldsymbol{r}'), \tag{50}$$

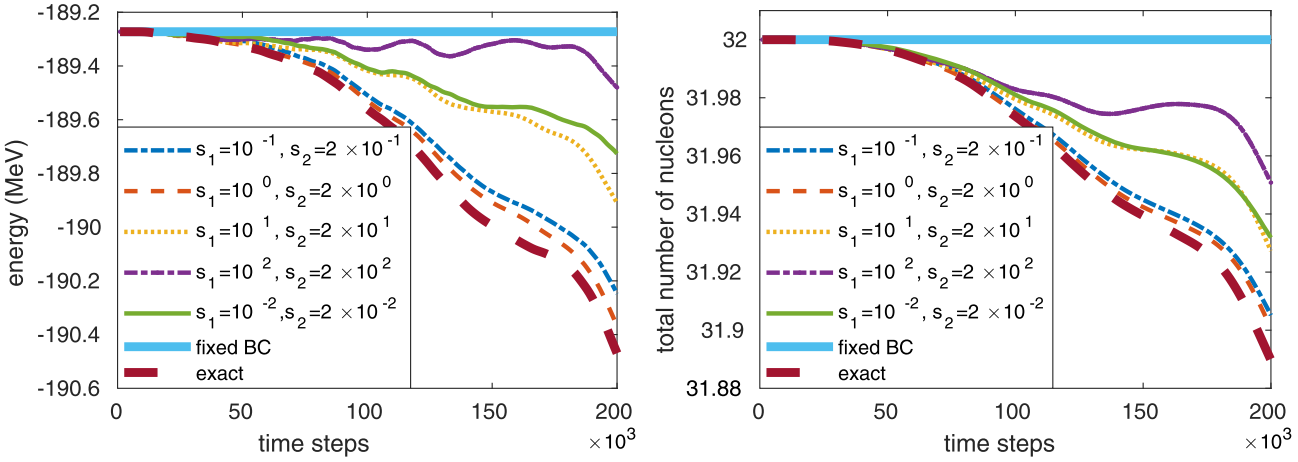

FIG. 6. The loss of nucleons and total energy.

and W_C is the Coulomb potential given by

$$W_C(\boldsymbol{r}) = e^2 \int d\boldsymbol{r}' \frac{1}{|\boldsymbol{r}-\boldsymbol{r}'|}\rho_p(\boldsymbol{r}'), \tag{51}$$

where V_0 and a are the coefficients of Yukawa interactions. ρ_p is the proton density. In practice, the Yukawa and Coulomb potentials are calculated by solving the corresponding Poisson and Helmholtz problems, respectively,

$$\begin{aligned} \nabla^2 W_c &= -2\pi e^2 \rho \\ (\nabla^2 - 1/a^2) W_Y &= -4\pi V_0 a \rho. \end{aligned} \tag{52}$$

We consider the above TDHF model (38) in the infinite region $\mathbb{R}^3$. In practice, the computational domain $\Omega_{\rm I}$ (usually a box) is only a small part of the entire Ω. We make the further assumption that

$$\psi_j = 0 \text{ for } i = 1, \ldots, A \text{ and } \rho = 0 \text{ in } \Omega_{\rm II}, \text{ at } t = 0. \tag{53}$$

Our approach starts from the discrete model. We denote $\boldsymbol{\varphi}_{\rm I}$ is the discretization of the wave function $\boldsymbol{\varphi}(\boldsymbol{x})$ in $\Omega_{\rm I}$. $H_{\rm II,II}$ is the discretization of the operator $-\frac{\hbar^2}{2m}\nabla^2$. $H_{\rm I,I}$ is still a nonlinear operator containing the Coulomb potential. The notations of boundaries and DtN map follow those in Sec. II. In this model, we only assume $\rho = 0$ in $\Omega_{\rm II}$ at $t = 0$.

As an application, we study the nuclear reaction of the $^{16}\mathrm{O} + {}^{16}\mathrm{O}$ system in the infinite space $\mathbb{R}^3$. The setup and data of the numerical experiments are mainly from Ref. [63]. In this model, we assume the perfect spin-isospin degeneracy for each particle, so that each spatial orbital is occupied by four nucleons. There are 32 nucleons in total in this system. The two particles at ground state are positioned in a box away from each other and away from the boundary. The ground state is achieved by solving the static Hartree-Fock equation self-consistently in $\Omega_{\rm I}$. We assume that there is no interaction between the two particles at the initial state. The Poisson and Helmholtz problems are solved by preconditioned conjugate gradient method using the same discretization method as the wave functions.

The initial condition is given by multiplying each orbital by the phase $e^{i\boldsymbol{k}\cdot\boldsymbol{r}}$ to create a head-on collision. Here $\boldsymbol{k}$ should be carefully selected to ensure the particles enter into the fusion window. Namely, two particles pass the Coulomb barrier and are trapped by the nuclear force. Otherwise, the two particles move to the boundaries and the nuclear fusion will not occur. We use the same integrator as the case for three-dimensional Schrödinger equation. The time step is set to be 0.001 fm/c. In each time step, we also need to perform the self-consistent iteration due to the nonlinearity [64,65].

In the numerical experiment, $\Omega_{\rm I}$ is discretized with grid spacing of 1 fm. The Laplacian operator is approximated by the seven-point scheme in each spatial direction. The region of interest is $[-15\text{ fm}, 15\text{ fm}]^3$. We employ the solution of a larger system ($[-30\text{ fm}, 30\text{ fm}]^3$) as the exact solution to examine the ABCs. The exact number of nucleons and the exact total energy are computed from the larger system restricted to the small region. The initial conditions of the two systems are the nucleon density at the ground state of the smaller system. One should notice that the ground state of the smaller system is not necessarily the ground state of the larger system. The initial condition of the larger system is not the ground state of itself. This will lead a small truncation error due to the long-range interaction in the system.

The energy conservation and mass conservation (Fig. 6) for the standard TDHF with Dirichlet boundary conditions are easily observed in our simulations. The system with ABCs released over 1 MeV from the total energy, and emitted 0.1 nucleons in the simulating period. More energy and nucleons are expected to be emitted over a longer period.

Our main focus here is to test how the absorbing property is influenced by the interpolation points. We present results from the following six cases: (A) $s_1 = 10^{-1}, s_2 = 2\times10^{-1}$; (B) $s_1 = 10^{0}, s_2 = 2\times10^{0}$; (C) $s_1 = 10^{1}, s_2 = 2\times10^{1}$; (D) $s_1 = 10^{2}, s_2 = 2\times10^{2}$; (E) $s_1 = 10^{-2}, s_2 = 2\times10^{-2}$; and (F) fixed boundary condition.

The case when $s_1 = 1$ and $s_2 = 2$ provides the best agreement with the exact solution in terms of both the number of nucleons and total energy. The case $s_1 = 0.1$ and $s_2 = 0.2$ follows second. When the order of magnitudes of s_1 and s_2 are much larger or smaller than 1, the absorbing properties are much worse. The optimal s_1 and s_2 should be on the order of 1. From Fig. 6, the absorbing property is not sensitive to the selection of s_1 and s_2, as long as we choose them in the interval [0.1, 1].

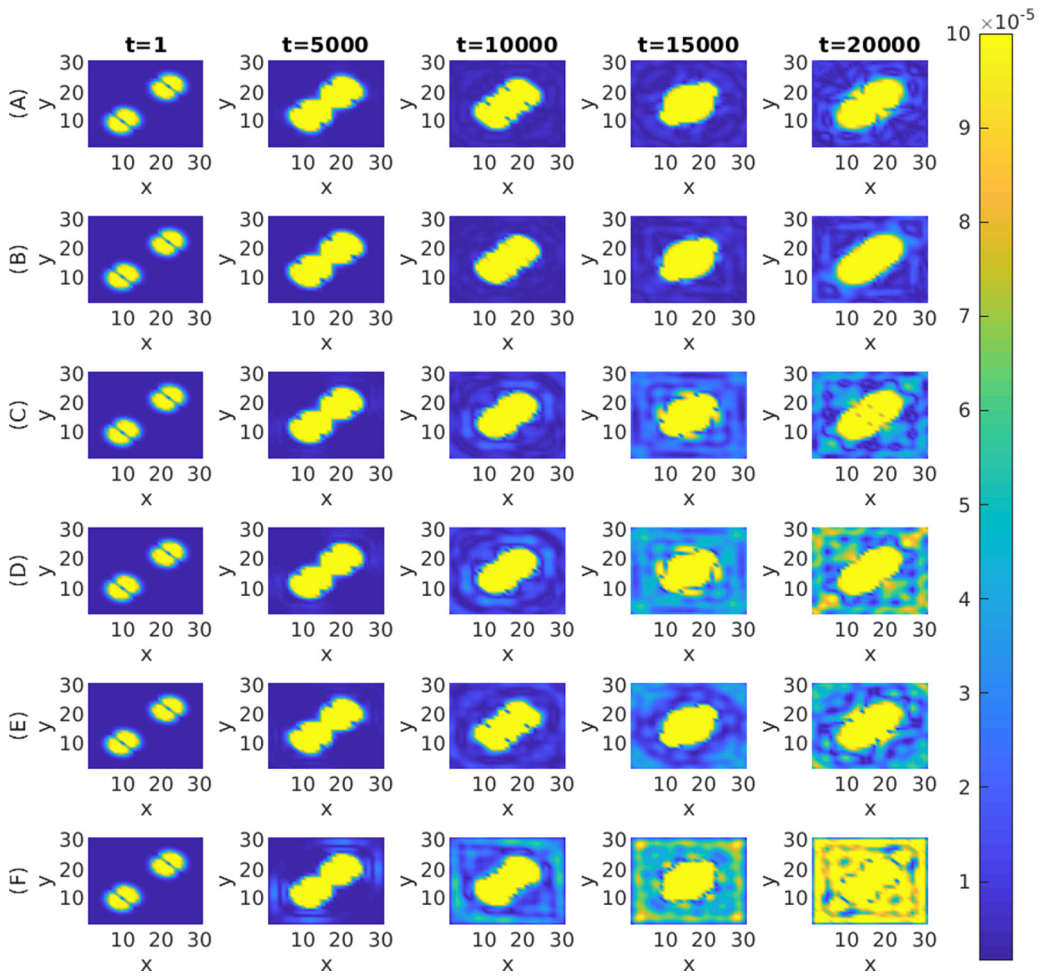

FIG. 7. Error of the nucleon density in time evolution of $^{16}O + {}^{16}O$ collision, projected onto the x-y plane. From the top to the bottom: (A) $s_1 = 10^{-1}$, $s_2 = 2 \times 10^{-1}$; (B) $s_1 = 10^{0}$, $s_2 = 2 \times 10^{0}$; (C) $s_1 = 10^{1}$, $s_2 = 2 \times 10^{1}$; (D) $s_1 = 10^{2}$, $s_2 = 2 \times 10^{2}$; (E) $s_1 = 10^{-2}$, $s_2 = 2 \times 10^{-2}$; (F) fixed boundary condition.

Further, we compare the profile of the densities with the exact solution. Results are displayed in Fig. 7. In the first 5000 time steps, the error of different cases are almost the same. However, when the wave function reaches the boundaries, the Dirichlet boundary condition generates massive errors as expected. The cases (A) and (B) still show great agreement with the exact density. The cases (C), (D), and (E) also improved the accuracy of density in varying degrees.

We note that the long-range potential (Coulomb and Yukawa) make the problem nonlinear in the entire space, in which case the ABCs are difficult to derive, unless further simplifications are made. However, since the two particles never propagate to the boundary, $\rho \approx 0$ outside. We expect that one can neglect the potential terms in the exterior.

V. SUMMARY AND DISCUSSIONS

We constructed absorbing boundary conditions for time-dependent Schrödinger equations by first deriving the Dirichlet-to-Neumann map. We chose the starting point to be a semidiscrete approximation so that the resulting boundary condition can be readily implemented with the discretization in the interior seamlessly. The nonlocality in time in the exact boundary condition is treated by rational interpolations of the Laplace transform, which in the time domain turns into linear ODEs. For the zeroth- and first-order approximations, the stability has been proved. The effectiveness and accuracy are also illustrated by various numerical tests. For higher-order absorbing boundary conditions, a direct proof seems rather challenging. Our numerical observations are that second-order and third-order methods are still stable for a wide range of interpolation points s.

In principle, the boundary conditions presented in this paper can be applied to three-dimensional problems with general geometry. The stability results do not depend on the specific configuration of the computational domain. However, a remaining challenge is to choose the *optimal* interpolation conditions to maximize the accuracy, i.e., minimize the reflection. For one-dimensional problems, or higher-dimensional problems in a half-plane, one can compute the reflection coefficients and choose the optimal boundary condition by minimizing the total reflection [69]. This approach breaks down when corners and edges are present. One possible remedy is the optimal interpolation strategy from order-reduction problems [70,71]. For instance, in the current setting, one can

formulate the following optimization problem:

$$s_0 = \arg\min \|K(s) - R_{1,1}(s)\|_{\mathcal{H}_2}, \tag{54}$$

for the first-order boundary condition to identify the *best* interpolation point. This will be pursued in separate works.

Another long-standing issue is associated with the long-range interactions among the electrons, i.e., the Coulomb interactions. This issue has been partially addressed in Ref. [72], where the Coulomb potential is replaced by an asymptotic form. But, in general, all the existing methods have not be constructed to take full account of the Coulomb potential.

APPENDIX A: EVALUATION OF THE DIRICHLET-TO-NEUMANN MAP

In this section, we briefly discuss the evaluation of the kernel [Eq. (16)] in the Laplace domain. The key is to use the Green's function to evaluate the selected inversion. We refer readers to our previous work [49,66] for the detailed derivations.

The discrete Green's function $\widetilde{G}_{ij}$ corresponding to the discretized operator $\widetilde{H}_{ij}$ satisfies

$$\sum_j \widetilde{H}_{i,j}\widetilde{G}_{jk} = \delta_{i,k}, \text{ for any integer } i, k.$$

To shorten the derivation, the notations of $\widetilde{G}_{\mathrm{I},\mathrm{II}}$ and $\widetilde{G}_{\mathrm{II},\mathrm{II}}$ follow the convention of $H_{\mathrm{I},\mathrm{II}}$ and $H_{\mathrm{II},\mathrm{II}}$, respectively. Furthermore, we introduce the boundary set in Ω_{II},

$$\Sigma = \{\boldsymbol{x}_j \in \Omega_{\mathrm{II}} | \text{ if there exists } \boldsymbol{x}_k \in \Omega_{\mathrm{I}} \text{ such that } H_{jk} \neq 0\}. \tag{A1}$$

and matrices

$$\widetilde{G}_{\Gamma,\Sigma} = [\widetilde{G}_{ij}]_{i\in\Gamma, j\in\Sigma}, \widetilde{G}_{\Sigma,\Sigma} = [\widetilde{G}_{ij}]_{i\in\Sigma, j\in\Sigma}, H_{\Gamma,\Sigma} = [H_{ij}]_{i\in\Gamma, j\in\Sigma}, H_{\Sigma,\Gamma} = [H_{ij}]_{i\in\Sigma, j\in\Gamma}.$$

We start with the discretized operator $\tilde{H}$ in Ω. By (11), the discretized operator satisfies

$$\widetilde{H}_{\mathrm{II},\mathrm{II}}\boldsymbol{\Phi}_{\mathrm{II}} + \widetilde{H}_{\mathrm{II},\mathrm{I}}\boldsymbol{\Phi}_{\mathrm{I}} = 0. \tag{A2}$$

The definition of the discrete Green's function implies that

$$\widetilde{G}_{\mathrm{II},\mathrm{II}}\widetilde{H}_{\mathrm{II},\mathrm{II}}\boldsymbol{\Phi}_{\mathrm{II}} + \widetilde{G}_{\mathrm{II},\mathrm{I}}\widetilde{H}_{\mathrm{I},\mathrm{II}}\boldsymbol{\Phi}_{\mathrm{II}} = \boldsymbol{\Phi}_{\mathrm{II}}. \tag{A3}$$

Equation (A2) and Eq. (A3) can now be combined into the following equation:

$$\boldsymbol{\Phi}_{\mathrm{II}} = \widetilde{G}_{\mathrm{II},\mathrm{I}}H_{\mathrm{I},\mathrm{II}}\boldsymbol{\Phi}_{\mathrm{II}} - \widetilde{G}_{\mathrm{II},\mathrm{II}}H_{\mathrm{II},\mathrm{I}}\boldsymbol{\Phi}_{\mathrm{I}}, \tag{A4}$$

where the fact that $\widetilde{H}_{\mathrm{I},\mathrm{II}} = H_{\mathrm{I},\mathrm{II}}$ has been used.

By multiplying both sides of (A4) by $H_{\Gamma,\mathrm{II}}$, we have

$$H_{\Gamma,\mathrm{II}}\boldsymbol{\Phi}_{\mathrm{II}} = H_{\Gamma,\mathrm{II}}\widetilde{G}_{\mathrm{II},\mathrm{II}}H_{\mathrm{I},\mathrm{II}}\boldsymbol{\Phi}_{\mathrm{II}} - H_{\Gamma,\mathrm{II}}\widetilde{G}_{\mathrm{II},\mathrm{II}}H_{\mathrm{II},\mathrm{I}}\boldsymbol{\Phi}_{\mathrm{I}}. \tag{A5}$$

Notice that $\boldsymbol{f}_\Gamma = H_{\Gamma,\mathrm{II}}\boldsymbol{\Phi}_{\mathrm{II}}$. Making use of the sparsity of $H_{\Gamma,\mathrm{II}}$ and $H_{\mathrm{I},\mathrm{II}}$, we obtain

$$\boldsymbol{f}_\Gamma = H_{\Gamma,\Sigma}\widetilde{G}_{\Sigma,\Gamma}\boldsymbol{f}_\Gamma - H_{\Gamma,\Sigma}\widetilde{G}_{\Sigma,\Sigma}H_{\Sigma,\Gamma}\boldsymbol{\Phi}_\Gamma. \tag{A6}$$

Therefore, the discrete Dirichlet-to-Neumann map is expressed as

$$\boldsymbol{f}_\Gamma = -(I_{n_\Gamma} - H_{\Gamma,\Sigma}\widetilde{G}_{\Sigma,\Gamma})^{-1}H_{\Gamma,\Sigma}\widetilde{G}_{\Sigma,\Sigma}H_{\Sigma,\Gamma}\boldsymbol{\Phi}_\Gamma. \tag{A7}$$

This shows that once the Green's function is available, the evaluation of the DtN map only involves the operations of small matrices.

APPENDIX B: DISCRETE GREEN'S FUNCTION FOR 1D SCHRÖDINGER EQUATION

Consider the one-dimensional time-dependent Schrödinger equation,

$$i\frac{\partial}{\partial t}\psi(t,x) + \frac{1}{2}\frac{\partial^2}{\partial x^2}\psi(t,x) = 0. \tag{B1}$$

By taking the Laplace transform in time ($t \to s$) and Fourier transform in space ($x \to q$), the corresponding fundamental solution solves

$$2siG(s,q) - q^2G(s,q) = 1, \tag{B2}$$

which gives

$$G(s,q) = \frac{1}{2si - q^2}. \tag{B3}$$

The inverse Fourier transform yields the fundamental solution in the Laplace domain

$$G(s,x) = -\frac{1}{2\sqrt{-2si}}e^{-\sqrt{-2si}|x|}. \tag{B4}$$

$G(s,x)$ is the continuous Green's function of the following equation in the Laplace domain. Now we turn to the discrete case. To obtain the discrete Green's function, we discretize the Schrödinger equation in the Laplace domain by the five-point scheme,

$$2si\psi_j(s) + \sum_{k=-2}^{2}\frac{c_k\psi_{j+k}(s)}{h^2} = 0, \tag{B5}$$

where $c_{-2} = -1/12$, $c_{-1} = 4/3$, $c_0 = -5/2$, $c_1 = 4/3$, and $c_2 = -1/12$. h is the grid spacing.

The characteristic equation of Eq. (B5) is given by

$$-\frac{1}{12}u^4 + \frac{4}{3}u^3 + \left(i2sh^2 - \frac{5}{2}\right)u^2 + \frac{4}{3}u - \frac{1}{12} = 0. \tag{B6}$$

The four roots of the characteristic equation are given by

$$\begin{aligned} u_1 &= 4 + a - \sqrt{6sh^2i + 8a + 24} \\ u_2 &= 4 - a + \sqrt{6sh^2i - 8a + 24} \\ u_3 &= 4 - a - \sqrt{6sh^2i - 8a + 24} \\ u_4 &= 4 + a + \sqrt{6sh^2i + 8a + 24}, \end{aligned} \tag{B7}$$

where $a = \sqrt{9 + 6sh^2i}$, $\mathrm{Re}(u_1) < 1$, and $\mathrm{Re}(u_3) < 1$ for a small s. We take the branch cut (u_1 and u_3) to ensure the boundedness of the Green's function. Hence, the discrete Green's function can be explicitly expressed as

$$G_j(s) = b_1u_1^{|j|} + b_2u_3^{|j|}, \tag{B8}$$

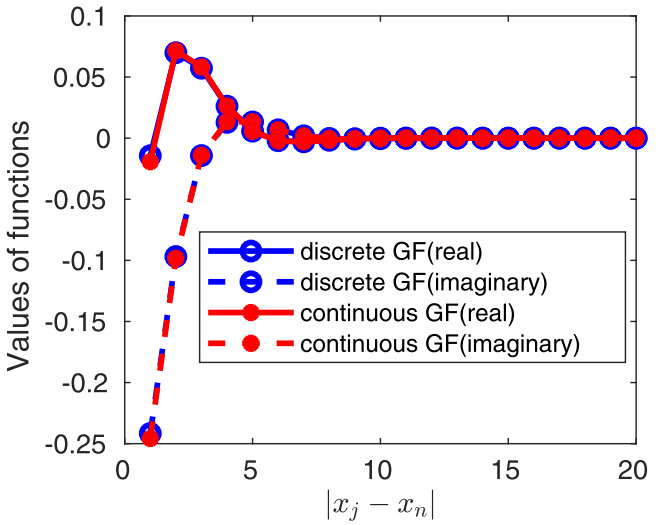

FIG. 8. One-dimensional discrete Green's function versus one-dimensional continuum Green's function, $s = 1, h = 1$.

where

$$b_1 = \frac{h^2}{2}\sqrt{\frac{3}{(3+2sh^2i)(24+6sh^2i+8a)}},$$
$$b_2 = \frac{h^2}{2}\sqrt{\frac{3}{(3+2sh^2i)(24+6sh^2i-8a)}}. \tag{B9}$$

The coefficients b_1 and b_2 are determined by the conditions

$$\sum_{j=-2}^{2} c_j u_j = 0 \text{ and } \sum_{j=-2}^{2} c_j u_j = 1.$$

We make a comparison between the continuum Green's function and analytical discrete Green's function in Fig. 8. Both the imaginary part and real part of the two Green's functions get close to each other when the distance gets large. This reveals that we can use the continuous Green's function to approximate the discrete Green's function when the distance is large, which becomes quite important especially when there is no explicit formula for the discrete Green's function.

APPENDIX C: FIRST-ORDER ABC FOR 1D SCHRÖDINGER EQUATION

Let us consider the 1D Schrödinger equation [Eq. (B1)] on the interval $\Omega_I = [x_l, x_r]$. We assume the discretization (B5) of Eq. (B1). $x_1, \ldots, x_N$ are N grid points inside the Ω_I. x_{-1}, x_0, x_{N+1}, and x_{N+2} are the exterior points. The input and output of the DtN map, respectively, are

$$\boldsymbol{f}_\Gamma = \begin{bmatrix} f_{-1} \\ f_0 \\ f_{N+1} \\ f_{N+2} \end{bmatrix} \quad \text{and} \quad \boldsymbol{\Phi}_\Gamma = \begin{bmatrix} \psi_{-1} \\ \psi_0 \\ \psi_{N+1} \\ \psi_{N+2} \end{bmatrix}. \tag{C1}$$

The matrices in the DtN map are explictly written as

$$H_{\Gamma,\Sigma} = \begin{bmatrix} 0 & -1/12 & 0 & 0 \\ -1/12 & 4/3 & 0 & 0 \\ 0 & 0 & 4/3 & 0 \\ 0 & 0 & -1/12 & 0 \end{bmatrix},$$
$$G_{\Sigma,\Gamma}(s) = \begin{bmatrix} G_2(s) & G_1(s) & G_N(s) & G_{N+1}(s) \\ G_3(s) & G_2(s) & G_{N-1}(s) & G_N(s) \\ G_N(s) & G_{N-1}(s) & G_2(s) & G_1(s) \\ G_{N+1}(s) & G_N(s) & G_1(s) & G_2(s) \end{bmatrix}$$

and

$$G_{\Sigma,\Sigma} = \begin{bmatrix} G_0(s) & G_1(s) & G_{N-2}(s) & G_{N-1}(s) \\ G_1(s) & G_0(s) & G_{N-3}(s) & G_{N-2}(s) \\ G_{N-2}(s) & G_{N-3}(s) & G_0(s) & G_1(s) \\ G_{N-1}(s) & G_{N-2}(s) & G_1(s) & G_0(s) \end{bmatrix}.$$

Therefore, the kernel function $K(s)$, which is defined by (15), can be evaluated (A7). Even for the 1D model, the DtN map is not trivial. To demonstrate the idea of the proposed ABCs, we determine the coefficients of the first-order ABC is by the moments of $K(s)$. More specifically, the coefficients of the first-order ABC are obtained by solving

$$(s_1 I - B)^{-1} A = K(s_1)$$
$$(s_1 I - B)^{-2} A = -K'(s_1) \tag{C2}$$

for certain $s_1 > 0$. Generally, the coefficients A and B cannot be explicitly expressed.

APPENDIX D: DISCRETE GREEN'S FUNCTION FOR THE 3D SCHRÖDINGER EQUATION

Consider the 3D time-dependent Schrödinger equation,

$$i\partial_t \psi(t, \boldsymbol{x}) + \tfrac{1}{2}\Delta\psi(t, \boldsymbol{x}) = 0. \tag{D1}$$

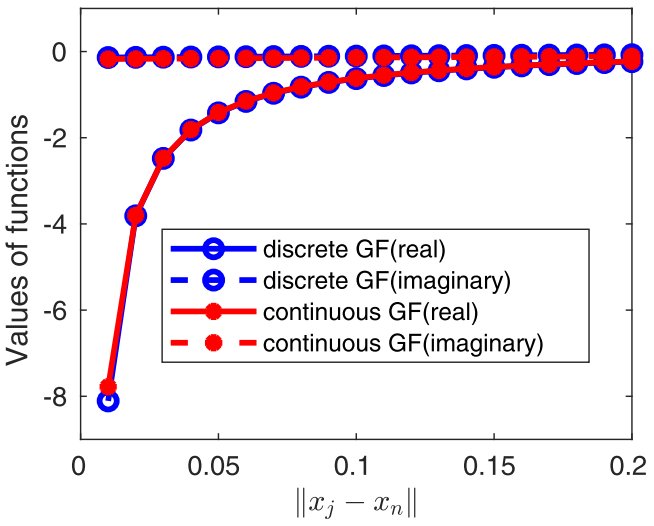

FIG. 9. Three-dimensional discrete Green's function and three-dimensional continuum Green's function, $h = 0.01, s = 10$.

By following the same procedure, the corresponding fundamental solution in the Laplace space is given by

$$G(\boldsymbol{x}, s) = -\frac{1}{4\pi r} e^{-\sqrt{-2si}r}, \tag{D2}$$

where $\boldsymbol{x} = (x_1, x_2, x_3)$ and $r = \sqrt{x_1^2 + x_2^2 + x_3^2}$.

For the finite-difference approximation, we discretize the operator, e.g., by the nine-point scheme in each spatial direction,

$$\frac{\partial^2 u}{\partial x^2} \approx \sum_{k=-4}^{4} \frac{c_k u_{j+k}}{h^2}. \tag{D3}$$

where $c_{-4} = -1/560$, $c_{-3} = 8/315$, $c_{-2} = -1/5$, $c_{-1} = 8/5$, $c_0 = 205/72$, $c_1 = 8/5$, $c_2 = -1/5$, $c_3 = 8/315$, and $c_4 = -1/560$. We denote c_k as the coefficients of the 3D discretization.

The discrete Green's function can be expressed as a Fourier integral,

$$G_{nj} = \frac{1}{|B|} \int_B \frac{e^{i(\boldsymbol{x}_n - \boldsymbol{x}_j)\cdot\boldsymbol{\xi}}}{C(\boldsymbol{\xi})} d\boldsymbol{\xi}, \quad C(\boldsymbol{\xi}) = \sum_{\boldsymbol{k}} c_{\boldsymbol{k}} e^{-i\boldsymbol{c}_{\boldsymbol{k}}\cdot\boldsymbol{\xi}}. \tag{D4}$$

Here B refers to the Fourier domain associated with the finite-difference grid points. It is given by $\frac{\pi}{h}[-1, 1] \times \frac{\pi}{h}[-1, 1] \times \frac{\pi}{h}[-1, 1]$ for uniform grids.

In Fig. 9, we show an example of the discrete Green's function, obtained by a quadrature with $100 \times 100 \times 100$ points in the Fourier domain, compared with the continuous Green's function.

[1] R. M. Martin, *Electronic Structure: Basic Theory and Practical Methods* (Cambridge University Press, Cambridge, 2011).

[2] T. Helgaker, P. Jorgensen, and J. Olsen, *Molecular Electronic-Structure Theory* (John Wiley & Sons, New York, 2014).

[3] H. Xie, Y. Kwok, F. Jiang, X. Zheng, and G. Chen, Complex absorbing potential based Lorentzian fitting scheme and time dependent quantum transport, J. Chem. Phys. **141**, 164122 (2014).

[4] K. Yabana, T. Nakatsukasa, J. I. Iwata, and G. F. Bertsch, Real-time, real-space implementation of the linear response time-dependent density-functional theory, Phys. Status Solidi B **243**, 1121 (2006).

[5] J. R. Hellums and W. R. Frensley, Non-Markovian open-system boundary conditions for the time-dependent Schrödinger equation, Phys. Rev. B **49**, 2904 (1994).

[6] A. Scrinzi, H. P. Stimming, and N. J. Mauser, On the non-equivalence of perfectly matched layers and exterior complex scaling, J. Comput. Phys. **269**, 98 (2014).

[7] Gy I. Szász, On the variational calculation of energies and widths of resonances, Phys. Lett. A **62**, 313 (1977).

[8] B. Simon, The definition of molecular resonance curves by the method of exterior complex scaling, Phys. Lett. A **71**, 211 (1979).

[9] C. W. McCurdy, M. Baertschy, and T. N. Rescigno, Solving the three-body Coulomb breakup problem using exterior complex scaling, J. Phys. B: At., Mol. Opt. Phys. **37**, R137 (2004).

[10] M. A. L. Marques, A. Castro, G. F. Bertsch, and A. Rubio, Octopus: A first-principles tool for excited electron–ion dynamics, Comput. Phys. Commun. **151**, 60 (2003).

[11] M. Tafipolsky and R. Schmid, A general and efficient pseudopotential Fourier filtering scheme for real space methods using mask functions, J. Chem. Phys. **124**, 174102 (2006).

[12] L.-W. Wang, Mask-function real-space implementations of nonlocal pseudopotentials, Phys. Rev. B **64**, 201107(R) (2001).

[13] U. V. Riss and H. D. Meyer, Investigation on the reflection and transmission properties of complex absorbing potentials, J. Chem. Phys. **105**, 1409 (1996).

[14] U. V. Riss and H. D. Meyer, Calculation of resonance energies and widths using the complex absorbing potential method, J. Phys. B: At., Mol. Opt. Phys. **26**, 4503 (1993).

[15] J. G. Muga, J. P. Palao, B. Navarro, and I. L. Egusquiza, Complex absorbing potentials, Phys. Rep. **395**, 357 (2004).

[16] E. A. Soloviev and S. I. Vinitsky, Suitable coordinates for the three-body problem in the adiabatic representation, J. Phys. B **18**, L557 (1985).

[17] E. Y. Sidky and B. D. Esry, Boundary-Free Propagation with the Time-Dependent Schrödinger Equation, Phys. Rev. Lett. **85**, 5086 (2000).

[18] U. V. Riss and H. D. Meyer, The transformative complex absorbing potential method: A bridge between complex absorbing potentials and smooth exterior scaling, J. Phys. B: At., Mol. Opt. Phys. **31**, 2279 (1998).

[19] F. He, C. Ruiz, and A. Becker, Absorbing boundaries in numerical solutions of the time-dependent Schrödinger equation on a grid using exterior complex scaling, Phys. Rev. A **75**, 053407 (2007).

[20] L. Tao, W. Vanroose, B. Reps, T. N. Rescigno, and C. W. McCurdy, Long-time solution of the time-dependent Schrödinger equation for an atom in an electromagnetic field using complex coordinate contours, Phys. Rev. A **80**, 063419 (2009).

[21] A. Scrinzi, Infinite-range exterior complex scaling as a perfect absorber in time-dependent problems, Phys. Rev. A **81**, 053845 (2010).

[22] J.-Y. Ge and J. Z. H. Zhang, Use of negative complex potential as absorbing potential, J. Chem. Phys. **108**, 1429 (1998).

[23] X. Li, Absorbing boundary conditions for time-dependent Schrödinger equations: A density-matrix formulation, J. Chem. Phys. **150**, 114111 (2019).

[24] X. Antoine, A. Arnold, C. Besse, M. Ehrhardt, and A. Schädle, A Review of artificial boundary conditions for the Schrödinger equation, Proc. Appl. Math. Mech. **7**, 1023201 (2007).

[25] H. Han and X. Wu, *Artificial Boundary Method* (Springer Science & Business Media, New York, 2013).

[26] H. Han and Z. Zhang, An analysis of the finite-difference method for one-dimensional Klein-Gordon equation on unbounded domain, Appl. Numer. Math. **59**, 1568 (2009).
[27] X. Antoine and C. Besse, Unconditionally stable discretization schemes of non-reflecting boundary conditions for the one-dimensional Schrödinger equation, J. Comput. Phys. **188**, 157 (2003).
[28] I. Alonso-Mallo and N. Reguera, Weak ILL-posedness of spatial discretizations of absorbing boundary conditions for Schrödinger-type equations, SIAM J. Numer. Anal. **40**, 134 (2003).
[29] I. Alonso-Mallo and N. Reguera, Adaptive absorbing boundary conditions for Schrödinger-type equations, in *Mathematical and Numerical Aspects of Wave Propagation (WAVES'03)*, edited by G. C. Cohen, P. Joly, E. Heikkola, and P. Neittaanmäki (Springer, Berlin, 2011), pp. 851–856.
[30] A. Arnold, On absorbing boundary conditions for quantum transport equations, ESAIM: Math. Modell. Numer. Anal. **28**, 853 (1994).
[31] A. M. Ermolaev, I. V. Puzynin, A. V. Selin, and S. I. Vinitsky, Integral boundary conditions for the time-dependent schrödinger equation: Atom in a laser field, Phys. Rev. A **60**, 4831 (1999).
[32] A. M. Ermolaev and A. V. Selin, Integral boundary conditions for the time-dependent schrödinger equation: Superposition of the laser field and a long-range atomic potential, Phys. Rev. A **62**, 015401 (2000).
[33] A. Arnold, M. Ehrhardt, and I. Sofronov, Discrete transparent boundary conditions for the Schrödinger equation: Fast calculation, approximation, and stability, Commun. Math. Sci. **1**, 501 (2013).
[34] S. Jiang and L. Greengard, Fast evaluation of nonreflecting boundary conditions for the Schrödinger equation in one dimension, Comput. Math. Appl. **47**, 955 (2004).
[35] T. Fevens and H. Jiang, Absorbing boundary conditions for the Schrödinger equation, SIAM J. Sci. Comput. **21**, 255 (2003).
[36] T. Shibata, Absorbing boundary conditions for the finite-difference time-domain calculation of the one-dimensional Schrödinger equation, Phys. Rev. B **43**, 6760 (1991).
[37] J. Szeftel, Design of absorbing boundary conditions for Schrödinger equations in $\mathbb{R}^d$, SIAM J. Numer. Anal. **42**, 1527 (2004).
[38] Z. Xu and H. Han, Absorbing boundary conditions for nonlinear Schrödinger equations, Phys. Rev. E **74**, 037704 (2006).
[39] S. Jiang and L. Greengard, Efficient representation of nonreflecting boundary conditions for the time-dependent Schrödinger equation in two dimensions, Commun. Pure Appl. Math. **61**, 261 (2008).
[40] X. Antoine, C. Besse, and V. Mouysset, Numerical schemes for the simulation of the two-dimensional Schrödinger equation using non-reflecting boundary conditions, Math. Comput. **73**, 1779 (2004).
[41] B. Alpert, L. Greengard, and T. Hagstrom, Nonreflecting boundary conditions for the time-dependent wave equation, J. Comput. Phys. **180**, 270 (2002).
[42] H. Han and Z. Huang, Exact artificial boundary conditions for the Schrödinger equation in $\mathbb{R}^2$, Commun. Math. Sci. **2**, 79 (2013).
[43] Z. Xu, H. Han, and X. Wu, Adaptive absorbing boundary conditions for Schrödinger-type equations: Application to nonlinear and multi-dimensional problems, J. Comput. Phys. **225**, 1577 (2007).
[44] J. P. Berenger, A perfectly matched layer for the absorption of electromagnetic waves, J. Comput. Phys. **114**, 185 (1994).
[45] C. Zheng, A perfectly matched layer approach to the nonlinear Schrödinger wave equations, J. Comput. Phys. **227**, 537 (2007).
[46] A. Bayliss and E. Turkel, Radiation boundary conditions for wave-like equations, Commun. Pure Appl. Math. **33**, 707 (1980).
[47] R. L. Higdon, Absorbing boundary conditions for difference approximations to the multidimensional wave equation, Math. Comput. **47**, 437 (1986).
[48] X. Antoine, C. Besse, and S. Descombes, Artificial boundary conditions for one-dimensional cubic nonlinear Schrödinger equations, SIAM J. Numer. Anal. **43**, 2272 (2006).
[49] X. Li, An atomistic-based boundary element method for the reduction of molecular statics models, Comput. Methods Appl. Mech. Eng. **225-228**, 1 (2012).
[50] E. J. Baerends, D. E. Ellis, and P. Ros, Self-consistent molecular Hartree-Fock-Slater calculations. I. The computational procedure, Chem. Phys. **2**, 41 (1973).
[51] M. A. L. Marques, C. A. Ullrich, F. Nogueira, A. Rubio, K. Burke, and E. K. U. Gross, *Time-dependent Density Functional Theory* (Springer Science & Business Media, Berlin, 2006), Vol. 706.
[52] V. A. Baskakov and A. V. Popov, Implementation of transparent boundaries for numerical solution of the Schrödinger equation, Wave Motion **14**, 123 (1991).
[53] D. Givoli, I. Patlashenko, and J. B. Keller, Discrete Dirichlet-to-Neumann maps for unbounded domains, Comput. Methods Appl. Mech. Eng. **164**, 173 (1998).
[54] X. Andrade, D. Strubbe, U. De Giovannini, A. H. Larsen, M. J. T. Oliveira, J. Alberdi-Rodriguez, A. Varas, I. Theophilou, N. Helbig, M. J. Verstraete, L. Stella, F. Nogueira, A. Aspuru-Guzik, A. Castro, M. A. L. Marques, and A. Rubio, Real-space grids and the Octopus code as tools for the development of new simulation approaches for electronic systems, Phys. Chem. Chem. Phys. **17**, 31371 (2015).
[55] P. Motamarri, M. R. Nowak, K. Leiter, J. Knap, and V. Gavini, Higher-order adaptive finite-element methods for Kohn–Sham density functional theory, J. Comput. Phys. **253**, 308 (2013).
[56] T. L. Beck, Real-space mesh techniques in density-functional theory, Rev. Mod. Phys. **72**, 1041 (2000).
[57] A. Quarteroni and A. Valli, *Domain Decomposition Methods for Partial Differential Equations*, Numerical Mathematics and Science (Clarendon Press, London, 1999).
[58] L. Lin, C. Yang, J. C. Meza, J. Lu, and L. Ying, SelInv—An algorithm for selected inversion of a sparse symmetric matrix, ACM Trans. Math. Softw. **37**, 40 (2011).
[59] Z. Bai, Krylov subspace techniques for reduced-order modeling of large-scale dynamical systems, Appl. Numer. Math. **43**, 9 (2002).
[60] P. Benner, S. Gugercin, and K. Willcox, A survey of projection-based model reduction methods for parametric dynamical systems, SIAM Rev. **57**, 483 (2015).

[61] G. A. Baker, G. A. Baker, Jr., G. A. Baker, Jr., P. Graves-Morris, and S. S. Baker, *Padé Approximants* (Cambridge University Press, Cambridge, 1996), Vol. 59.

[62] X. Li, On the stability of boundary conditions for molecular dynamics, J. Comput. Appl. Math. **231**, 493 (2009).

[63] H. Flocard, S. E. Koonin, and S. Weiss, Hartree-Fock calculations: Application to $^{16}O + ^{16}O$ collisions, Phys. Rev. C **17**, 1682 (1978).

[64] A. Castro, M. A. L. Marques, and A. Rubio, Propagators for the time-dependent Kohn–Sham equations, J. Chem. Phys. **121**, 3425 (2004).

[65] A. G. Pueyo, M. A. L. Marques, A. Rubio, and A. Castro, Propagators for the time-dependent Kohn-Sham equations: Multistep, Runge-Kutta, exponential Runge-Kutta, and commutator free Magnus methods, J. Chem. Theory Comput. **14**, 3040 (2018).

[66] X. Wu and X. Li, Stable absorbing boundary conditions for molecular dynamics in general domains, Comput. Mech. **62**, 1259 (2018).

[67] S. E. Koonin, K. T. R. Davies, V. Maruhn-Rezwani, H. Feldmeier, S. J. Krieger, and J. W. Negele, Time-dependent Hartree-Fock calculations for $^{16}O + ^{16}O$ and $^{40}Ca + ^{40}Ca$ reactions, Phys. Rev. C **15**, 1359 (1977).

[68] V. Maruhn-Rezwani, K. T. R. Davies, and S. E. Koonin, Time-dependent Hartree-Fock calculations for $^{14}N + ^{12}C$ reactions, Phys. Lett. B **67**, 134 (1977).

[69] X. Li and E. Weinan, Variational boundary conditions for molecular dynamics simulations of solids at low temperature, Commun. Comput. Phys. **1**, 135 (2006).

[70] B. Anic, An interpolation-based approach to the weighted-$\mathcal{H}_2$ model reduction problem, Ph.D. thesis, Virginia Tech, 2008.

[71] S. Gugercin, A. Antoulas, and C. Beattie, $\mathcal{H}_2$ model reduction for large-scale linear dynamical systems, SIAM J. Matrix Anal. Appl. **30**, 609 (2008).

[72] M. Ehrhardt and A. Zisowsky, Fast calculation of energy and mass preserving solutions of Schrödinger–Poisson systems on unbounded domains, J. Comput. Appl. Math. **187**, 1 (2006).